ELSEVIER

Since January 2020 Elsevier has created a COVID-19 resource centre with free information in English and Mandarin on the novel coronavirus COVID-19. The COVID-19 resource centre is hosted on Elsevier Connect, the company's public news and information website.
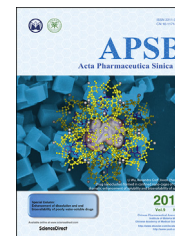
ORIGINAL ARTICLE

Schaftoside inhibits 3CLpro and PLpro of SARS-CoV-2 virus and regulates immune response and inflammation of host cells for the treatment of COVID-19

Yang Yi[a,†], Meng Zhang[a,†], Heng Xue[b,c,†], Rong Yu[a], Yang-Oujie Bao[a], Yi Kuang[a], Yue Chai[a], Wen Ma[a], Jing Wang[a], Xiaomeng Shi[a], Wenzhe Li[a], Wei Hong[b,c], Junhua Li[b,c], Elishiba Muturi[b,c], Hongping Wei[b,c], Joachim Wlodarz[d], Szczepan Roszak[e], Xue Qiao[a,*], Hang Yang[b,c,*], Min Ye[a,*]

[a]State Key Laboratory of Natural and Biomimetic Drugs, School of Pharmaceutical Sciences, Peking University, Beijing 100191, China
[b]CAS Key Laboratory of Special Pathogens and Biosafety, Center for Biosafety Mega-Science, Wuhan Institute of Virology, Chinese Academy of Sciences, Wuhan 430071, China
[c]University of Chinese Academy of Sciences, Beijing 100049, China
[d]Faculty of Science and Technology, University of Silesia, Katowice 40-007, Poland
[e]Department of Physical and Quantum Chemistry, Faculty of Chemistry, Wroclaw University of Science and Technology, Wroclaw 50-370, Poland

Abstract   It is an urgent demand worldwide to control the coronavirus disease 2019 (COVID-19) pandemic caused by the severe acute respiratory syndrome coronavirus 2 (SARS-CoV-2) virus. The 3-chymotrypsin-like protease (3CLpro) and papain-like protease (PLpro) are key targets to discover SARS-CoV-2 inhibitors. After screening 12 Chinese herbal medicines and 125 compounds from licorice, we found that a popular natural product schaftoside inhibited 3CLpro and PLpro with IC_{50} values of 1.73 ± 0.22 and 3.91 ± 0.19 µmol/L, respectively, and inhibited SARS-CoV-2 virus in Vero E6 cells with EC_{50} of 11.83 ± 3.23 µmol/L. Hydrogen−deuterium exchange mass spectrometry analysis, quantum

*Corresponding authors. Tel./fax: +86 10 82801516 (Min Ye).
   E-mail addresses: qiaoxue@bjmu.edu.cn (Xue Qiao), yangh@wh.iov.cn (Hang Yang), yemin@bjmu.edu.cn (Min Ye).
   †These authors made equal contributions to this work.

mechanics/molecular mechanics calculations, together with site-directed mutagenesis indicated the anti-viral activities of schaftoside were related with non-covalent interactions with H41, G143 and R188 of 3CL^{pro}, and K157, E167 and A246 of PL^{pro}. Moreover, proteomics analysis and cytokine assay revealed that schaftoside also regulated immune response and inflammation of the host cells. The anti-inflammatory activities of schaftoside were confirmed on lipopolysaccharide-induced acute lung injury mice. Schaftoside showed good safety and pharmacokinetic property, and could be a promising drug candidate for the prevention and treatment of COVID-19.

1. Introduction

Currently, it is a world-wide urgent requirement to control the pandemic of the coronavirus disease 2019 (COVID-19) caused by the severe acute respiratory syndrome coronavirus 2 (SARS-CoV-2). Since its first report in late 2019, COVID-19 has caused over 6.30 million deaths globally as of June 2022[1,2]. While vaccines have been developed, SARS-CoV-2 variants exhibit higher infectivity and contain mutations that cause partial immune escape[3].

The major therapeutic targets to discover SARS-CoV-2 inhibitors include 3-chymotrypsin-like protease (3CL^{pro} or M^{pro}, nsp5) and papain-like protease (PL^{pro}, nsp3). The 3CL^{pro} is a highly conserved cysteine protease indispensable for coronavirus replication[4]. It processes two viral polyproteins pp1a and pp1ab into 16 non-structural proteins, which engage in the production of subgenomic RNAs to encode four main structural proteins[5−9]. PL^{pro} plays an important role in viral maturation, dysregulation of host inflammation, and antiviral immune responses[10−12]. As the crystal structures of SARS-CoV-2 3CL^{pro} and PL^{pro} have been resolved[6,10], a number of small molecule inhibitors have been reported. For instance, **11a** (IC$_{50}$, 0.053 µmol/L against 3CL^{pro}; EC$_{50}$, 0.53 µmol/L against SARS-CoV-2 virus) and **11b** (IC$_{50}$, 0.040 µmol/L; EC$_{50}$, 0.72 µmol/L) formed covalent bonding with Cys145 of 3CL^{pro} (M^{pro}) through an aldehyde group[6]. Other potent 3CL^{pro} inhibitors include **GC376** (IC$_{50}$, 0.15 µmol/L; EC$_{50}$, 0.70 µmol/L)[7], **MI30** (IC$_{50}$, 17.2 nmol/L; EC$_{50}$, 0.54 µmol/L in Vero E6 cells and 1.1 nmol/L in HPAEpiC cells), and **PF07321332** (IC$_{50}$, 3.11 nmol/L; EC$_{50}$, 74.5 nmol/L)[8,9]. Only a few PL^{pro} inhibitors have been reported including **GRL0617** (IC$_{50}$, 2.2 µmol/L; EC$_{50}$, 21 µmol/L)[10−12].

Recently, molnupiravir and paxlovid [nirmatrelvir (PF-07321332) tablets and ritonavir tablets] have been approved as the first small molecule oral drugs for the treatment of COVID-19. They reduced the risk of hospitalization or death by 50% and 89%, respectively[13,14]. However, their prices are high, around 700 and 500 US dollars for five days treatment, respectively[15,16]. Molnupiravir must be given within five days after symptoms appear, and it is ineffective if it is taken after the patient is hospitalized[13−16]. Therefore, it is still highly demanded to develop effective and less expensive drugs against COVID-19.

Aside from synthetic chemicals, traditional Chinese medicines can ameliorate clinical symptoms of COVID-19 and lower the risk of in-hospital mortality, and have been widely used for the prevention and treatment of COVID-19 in China[17−19]. However, only a few bioactive phytochemicals have been discovered from Chinese herbal medicines, thus far, though natural products are an important source for drug discovery. Salvianolic acid C (EC$_{50}$,

3.41 µmol/L) from *Salvia miltiorrhiza*[20] and kobophenol A (EC$_{50}$, 71.6 µmol/L) from *Caragana sinica*[21] inhibited SARS-CoV-2 infection by blocking the formation of six-helix bundle core of spike protein and the interaction between the ACE2 receptor and S1-RBD, respectively. Recently, Su et al.[4] reported that myricetin (EC$_{50}$, 8.0 µmol/L) and dihydromyricetin (EC$_{50}$, 13.5 µmol/L) inhibited the SARS-CoV-2 3CL^{pro} with IC$_{50}$ of 0.63 and 1.14-µmol/L, respectively.

In the present work, we screened 12 frequently used Chinese herbal medicines and 125 compounds from licorice for their inhibitory activities against SARS-CoV-2 3CL^{pro} and PL^{pro} by enzymatic and antiviral assays. We discovered that schaftoside can be a potent 3CL^{pro}/PL^{pro} dual-target SARS-CoV-2 inhibitor, and also remarkably regulate immune response and inflammation of host cells in a mice model.

2. Materials and methods

2.1. Chemicals and reagents

All licorice compounds were purified by our laboratory from the roots and rhizomes of *Glycyrrhiza uralensis* Fisch[22]. **GC376** and **GRL0617** were purchased from Shanghai Yuanye Bio-Technology Co., Ltd. Dabcyl-KTSAVLQSGFRKME-Edans and (E-EDANS)RELNGGAPI(K-DABCYL)S were synthesized from GL Biochem (Shanghai) Ltd. SARS-CoV-2 3CL^{pro} and PL^{pro} were respectively purchased from Novoprotein Technology Co., Ltd., and Sino Biological Inc. IL-1, IL-1β, IL-6, IL-7, IL-8, TNF-α, IFN-β, and IFN-γ were measured by ELISA kits from MEIMIAN (www.mmbio.cn). Antibodies of IL-1β, IL-6, and TNF-α were purchased from ABCAM (https://www.abcam.cn). The animal facilities and protocols were approved by the Animal Care and Use Committee of Peking University Health Science Center (SYXK 2016-0041). All animal care and experimental procedures in this work were in accordance with Guide for the Care and Use of Laboratory Animals (National Institutes of Health).

2.2. Herbal materials and extracts

The Chinese herbal medicines were purchased from Beijing Tong-Ren-Tang drug store. A total of 12 herbal medicines were studied, including Isatidis Radix (Ban-Lan-Gen), Ephedrae Herba (Ma-Huang), Astragali Radix (Huang-Qi), Glycyrrhizae Radix et Rhizoma (Gan-Cao), Lonicerae Flos (Jin-Yin-Hua), Scutellariae Radix (Huang-Qin), Forsythiae Fructus (Lian-Qiao), Platycodonis Radix (Jie-Geng), Armeniacae Semen Amarum (Ku-Xing-Ren), Atractylodis Macrocephalae Rhizoma (Bai-Zhu), Pogostemonis

Herba (Guang-Huo-Xiang), and Citri Reticulatae Pericarpium (Chen-Pi). To prepare the herbal extracts, the powder (5 g) of each herb was extracted with 50 mL of 95% ethanol in a water bath at 90 °C for 30 min for three times. The extract was concentrated and then freeze dried.

2.3. Protein expression, purification, and crystallization

The full-length cDNA of SARS-CoV-2 3CL^{pro} (Genbank No. MN908947.3) was cloned into the pET28a vector. A 6 × His tag followed by TEV protease cleavage sequence was added before the N-terminus of the target protein to facilitate purification. The His-TEV-3CL^{pro} protein was expressed in *Escherichia coli* BL21(DE3) strain and purified by Ni-NTA affinity chromatography. After purification, the recombinant protein was digested by TEV protease to cut the His tag. The sample was added onto Ni-NTA affinity beads for the second time to purify the protein. The flow-through was concentrated and then applied to size-exclusion chromatography on a Superdex 200 increase 10/300 GL pre-packed column for further purification. The elution buffer was 10 mmol/L Tris−HCl pH 7.5 and 100 mmol/L NaCl. Fractions containing 3CL^{pro} were collected and concentrated to 10 mg/mL (Supporting Information Fig. S1). Crystals of 3CL^{pro} were obtained after 5 days at 16 °C in hanging drops containing 2 μL of protein solution and 2 μL of reservoir solution (0.05 sodium citrate tribasic dihydrate, 0.12 mol/L potassium chloride, 0.08 mol/L Bis−Tris, 14% PEG 4000, pH = 6.0). The crystals were frozen in a reservoir solution with 30% glycerol.

2.4. Enzymatic activity assay

The proteolytic activity of SARS-CoV-2 3CL^{pro} and PL^{pro} were measured using the fluorogenic substrate Dabcyl-KTSAVLQ-SGFRKME-Edans and (E-EDANS)RELNGGAPI(K-DABCYL)S, respectively (https://www.novoprotein.com.cn/). The reaction mixture contained 12.5 μg/mL purified enzyme, 50 μg/mL herbal extract or 8 μmol/L pure compound, 20 mmol/L Tris−HCl buffer (pH 7.0) for 3CL^{pro} or 50 mmol/L HEPES (pH 7.5) buffer for PL^{pro}, and 3 mmol/L substrate for 3CL^{pro} or 5 mmol/L substrate for PL^{pro}. The inhibition kinetics for both 3CL^{pro} and PL^{pro} were determined at a constant substrate concentration with different concentrations of samples (1, 2, 4, 8, and 16 μmol/L). The reactions were conducted at 25 °C with continuous monitoring of fluorescence for 10 min. The enzyme activity was demonstrated by monitoring the increase of emission fluorescence at 535 nm upon excitation at 340 nm on a FlexStation 3 Multi-Mode Microplate Reader. The activity was calculated according to the following equation[23,24]:

$$A = ((\Delta OD_{test})df)/(\Delta OD_{control}(2.204092 \times C \times V_s))$$

where A is enzyme activity, df is dilution factor, ΔOD is absorption change/min, V_s is sample volume, and C is concentration of 3CL^{pro}.

2.5. Surface plasmon resonance (SPR) assay

The binding affinity of samples to SARS-CoV-2 3CL^{pro}, PL^{pro}, and their mutants were determined using the SPR biosensor technology (Biacore 8K). The protein was immobilized onto the sensor chip CM5 by the standard primary amine coupling reaction. SARS-CoV 3CL^{pro}, PL^{pro}, and their mutants were diluted with 10 mmol/L sodium acetate (pH 4.5) to 25 μg/mL. The final

immobilized level was typically above 10,000 RU. The compounds were injected as analytes at various concentrations at a flow rate of 30 μL/min with a contact time of 60 s and a dissociation time of 60 s, using PBS containing 5% DMSO and 0.05% Surfactant P20 as running buffer. Data were analyzed by the Biacore evaluation software. The equilibrium dissociation constants (K_D) evaluating the protein−ligand binding affinity were determined by kinetics analysis of the Biacore data.

2.6. Cell viability assay

Cell Counting Kit-8 (CCK-8, Dojindo, Japan) assay was conducted to determine cell viability. Briefly, Vero E6 cells were seeded in 96-well plates at a density of 1×10^4 cells per well (in DMEM + 10% FBS), and were incubated for 24 h at 37 °C, 5% CO$_2$. Then, the compounds (maximum concentration at 200 μmol/L, <1% DMSO) were diluted in DMEM culture medium containing 10% FBS and were added to each well. The organic solvent in DMEM was less than 0.1%. After 24 h, contents of the wells were replaced with fresh medium containing 10% CCK-8 solution and were incubated at 37 °C for 3 h. The final optical density at OD$_{450}$ was measured using a Synergy H1 Microplate Reader.

2.7. Antiviral assay

Vero E6 cells were co-cultured with various concentrations of drugs overnight in 24-well plates at a density of 1×10^5 cells/well, and then infected by SARS-CoV-2 (nCoV-2019BetaCoV/Wuhan/WIV04/2019) at a multiplicity of infection (MOI) of 0.01. After 24 h of infection, RNA was extracted from the cell supernatant according to the manufacturer's instructions using QIAamp viral RNA mini kit (Qiagen, 52906). qRT-PCR was used to quantify the viral RNA with primers *ORF1ab*-F (5′-CCCTGTGGGTTTTACACTTAA-3′) and *ORF1ab*-R (5′-ACGATTGTGCATCAGCTGA-3′) combined with the probe 5′-FAM-CCGTCTGCGGTATGTGGAAAGGTTATGG-BHQ1-3′ by Luna Universal Probe One-Step RT-PCR Kit (Invitrogen, E3006).

2.8. Immunofluorescence assay

Vero E6 cells were seeded on Biocoat Coverslips for 24 h and then infected with SARS-CoV-2 in the presence of 10 or 30 μmol/L of schaftoside. After 24 h of infection, cells were fixed with 4% paraformaldehyde for 15 min. Cells were incubated with 1:1000 diluted primary antibody against the spike protein of SARS-CoV-2 for 1 h. After a thorough wash for 15 min to remove unbound antibodies, cells were then incubated with 1:500 diluted FITC-labeled goat anti-rabbit IgG antibodies (ThermoFisher Scientific, Invitrogen) for 1 h. The coverslips were washed for another 15 min, followed by nuclei staining with 4,6-diamidino-2-phenylindole (DAPI, Sigma), and then imaged by a confocal fluorescence microscope (PerkinElmer, UltraVIEW VoX, USA).

2.9. Hydrogen−deuterium exchange mass spectrometry (HDX-MS) analysis

Deuterium labeling was initiated with a 20-fold dilution into D$_2$O buffer (100 mmol/L phosphate, pH 7.0) of 3CL^{pro} protein (1 mg/mL), 3CL^{pro} (1 mg/mL) with schaftoside (1 mmol/L), PL^{pro} protein (1 mg/mL), or PL^{pro} (1 mg/mL) with schaftoside (1 mmol/L). After 0.25, 0.5, and 10 min of labeling, the labeling

reaction was quenched with the addition of quenching buffer (100 mmol/L phosphate, 4 mol/L GdHCl, 0.5 mol/L TCEP, pH 2.0). Samples were then injected and online digested using a Waters ENZYMATE BEH pepsin column (2.1 mm × 30 mm, 5 μm). The peptides were trapped and desalted on a VanGuard Pre-Column trap (ACQUITY UPLC BEH C18, 1.7 μm) for 3 min, eluted from the trap using 15% acetonitrile at a flow rate of 100 μL/min, and then separated using an ACQUITY UPLC BEH C18 column (1.0 mm × 100 mm, 1.7 μm). All mass spectra were acquired on a Waters Xevo G2 mass spectrometer. Peptides from an unlabeled protein were identified using ProteinLynx Global Server (PLGS) searches of a protein database including 3CL^pro and PL^pro sequences only. Relative deuterium levels for each peptide were calculated by subtracting the mass of the undeuterated control sample from that of the deuterium-labeled sample. All mass spectra were processed using DynamX 3.0 (Waters Corporation). Deuterium levels were not corrected for back exchange and thus reported as relative.

2.10. Docking and quantum mechanics/molecular mechanics (QM/MM) simulations

Molecular structures of the natural product ligands were optimized by B3LYP/6-311G(d) method[25−27]. The crystal structure of 3CL^pro (PDB ID: 6LZE)[6] and PL^pro (7CJM)[10] were used as a reference for protein−ligand system. Docking calculations were performed by AutoDock Vina and AutoDocktools v1.5.6 software[28]. The extracted complex of the ligand and amino acid residues from molecular docking was optimized by QM/MM simulations. The QM atoms from schaftoside, H41, G143, C145, R188 and Q192 of 3CL^pro, and K157, E167, A246 and Y268 of PL^pro were described by DFT method B3LYP at 6-311G basis set, while the MM atoms from T25, T26, M49, M162, H163, F140, N142, H164, M165, E166, P168, D187 and Q189 of 3CL^pro, and D164, P247, P248, Y264, Q269, Y273 and T301 of PL^pro were simulated by the UFF force field[29]. The calculations were performed using the Gaussian16 suite of codes[30].

2.11. Site-directed mutagenesis

Site-directed mutagenesis of 3CL^pro and PL^pro, including H41A, G143A and R188A mutants of 3CL^pro, and K157A, E167A and Y268A mutants of PL^pro, were constructed using Fast Mutagensis System kit (Transgen, China) according to the manufacturer's instructions. The primer pairs designed to construct the mutants are listed in Supporting Information Table S1. Enzyme assays of the mutated recombinant proteins were conducted under the same conditions as described above for native proteins (Fig. S1).

2.12. Proteomics analysis

Vero E6 cells were infected with SARS-CoV-2 virus, or with schaftoside (30 μmol/L) and SARS-CoV-2 for 24 h (MOI = 1), respectively. The samples were sonicated using a high intensity ultrasonic processor (Scientz) in lysis buffer (8 mmol/L urea, 1% protease inhibitor cocktail). The debris was removed by centrifugation. For the first digestion overnight, trypsin was added at 1:50 trypsin-to-protein mass ratio. Each channel of peptide was labeled by their respective TMT reagent (based on manufacturer's protocol, ThermoFisher Scientific), and incubated for 2 h at room temperature. The pooled samples were desalted with a Strata X C18 SPE column (Phenomenex) and dried by vacuum centrifugation. The

tryptic peptides were dissolved in solvent A (0.1% formic acid and 2% acetonitrile in water), directly loaded onto a home-made reversed-phase analytical column (25 cm length, 75 μm i.d.). Peptides were separated with a gradient from 5% to 25% solvent B (0.1% formic acid in 90% acetonitrile) over 60 min, 25%−35% in 22 min, up to 80% in 4 min, and then held at 80% for 4 min, all at a constant flow rate of 450 nL/min on an EASY-nLC 1200 UPLC system (ThermoFisher Scientific). The separated peptides were characterized by a Q Exactive HF-X mass spectrometer (ThermoFisher Scientific) with a nano-electrospray ion source.

GO annotation proteome was derived from the UniProt-GOA database (http://www.ebi.ac.uk/GOA/). Proteins were classified by Gene Ontology annotation based on three categories: biological process, cellular component, and molecular function. For functional enrichment, proteins were classified by GO biological process annotation. A two-tailed Fisher's exact test was employed to test the enrichment of the differentially expressed protein against all identified proteins. The GO with P value < 0.05 was considered significant.

2.13. Lipopolysaccharide (LPS)-induced acute lung injury (ALI) mice model

Male BALB/c mice (20 g) were provided by the Experimental Animal Center of Peking University Health Science Center (Beijing, China). Mice in the blank, control, and schaftoside groups were respectively administered with saline solution, LPS (2 mg/kg, i.n., intranasal administration), and LPS (2 mg/kg, i.n.) coupled with schaftoside (10, 20 mg/kg, i.g.). After 8 h of LPS administration, blood samples and lung tissues were collected.

2.14. Pathological analysis

Small pieces were obtained from lung tissues of the ALI model and fixed in 4% paraformaldehyde. Proper fixing was followed by dehydration of the specimens in graded ethanol, clearing in xylene, embedding in paraplast, and sectioning at 5-μm thickness. The sections were stained using the HE staining method to demonstrate the histological structure of testes in control, model, and schaftoside-treated mice. Images were taken using WISLEAP (WS-10).

2.15. Immunohistochemistry (IHC)

The lung tissue sections of ALI model were analyzed by IHC. After incubation with 3% H_2O_2 for 10 min, antigen retrieval was performed by incubating the samples in citrate buffer (pH 8.0) for 5 min high heat, and 15 min low heat. After blocking with goat serum, sections were incubated for 2 h with primary antibodies (Abcam, TNF-α, 1:20; IL-6, 1:50; IL-1β, 1:250). Sections were washed three times with phosphate-buffered saline and incubated with HRP goat anti-mouse IgG. After three times washing with phosphate-buffered saline, DAB was incubated for 2 min. Then, we stopped the reaction and stained using hematoxylin. Images were taken using WISLEAP (WS-10).

2.16. Acute toxicity test in mice

Male ICR mice (20 g) were randomly and evenly distributed into four groups ($n = 5$), including control (distilled water, i.g.) and different dosing groups (20, 40, and 300 mg/kg). Animals were treated for 7 days.

2.17. Statistical analysis

All the data are expressed as mean $\pm$ standard deviation (SD) and were analyzed using SPSS 20.0. Significant differences between groups were assessed by Student's t-test and one-way ANOVA. Differences were considered statistically significant at $P < 0.05$.

3. Results

3.1. Enzymatic activity assay and molecular docking

We tested the 12 most frequently used herbal medicines for the treatment of COVID-19 in China for their inhibitory activities against 3CL^{pro} and PL^{pro} (Fig. 1A)[31]. Of the herbal extracts (50 μg/mL), Isatidis Radix (BLG), Ephedrae Herba (MH), Astragali Radix (HQ1), and Glycyrrhizae Radix et Rhizoma (licorice, GC) showed the most potent activities against 3CL^{pro}, with inhibition rates of 38.17%, 37.76%, 34.70%, and 32.85%, respectively (Fig. 1B and Supporting Information Table S2). Among them, licorice also showed high inhibitory activity against PL^{pro} with an inhibition rate of 40.93% (Supporting Information Table S3). Thus, we focused on licorice for follow-up studies.

Using AutoDock VINA, we conducted a virtual screening of 125 compounds we previously isolated from licorice (the roots and rhizomes of *G. uralensis*)[22]. The binding energies with 3CL^{pro} and PL^{pro} were determined using SARS-CoV-2 3CL^{pro} (PDB ID: 6LZE)[6] and PL^{pro} (7CJM)[10] crystal structures (Fig. 1C and Supporting Information Fig. S2), respectively. Finally, 17 compounds (**1–17**) for 3CL^{pro} and 7 compounds (**8–23**) for PL^{pro} with binding affinity energy below −8.0 kcal/mol were discovered (Supporting Information Tables S4 and S5).

The above compounds were then evaluated by enzymatic assays. At 8 μmol/L, schaftoside (**1**), vicenin-2 (**2**), and licoisoflavanone (**3**) could inhibit 3CL^{pro} by 75.9%, 76.53%, and 66.86%, respectively, with 82.29% for the positive control **GC376** (Fig. 1D). Interestingly, schaftoside also demonstrated potent activity against PL^{pro} with an inhibition rate of 60% at 8 μmol/L (positive control **GRL0617**, 84.75%) (Fig. 1E). The chemical structures are given in Fig. 1F and Supporting Information Fig. S3. The IC$_{50}$ values of schaftoside (1.73 $\pm$ 0.22 μmol/L), vicenin-2 (1.43 $\pm$ 0.20 μmol/L), and licoisoflavanone (1.52 $\pm$ 0.14 μmol/L) against 3CL^{pro}, and that of schaftoside (3.91 $\pm$ 0.19 μmol/L) against PL^{pro} were all below 5 μmol/L (Fig. 2A and B). Moreover, schaftoside at 8 μmol/L also inhibited the 3CL^{pro} and PL^{pro} proteins of SARS-CoV, with inhibition rates of 68.4% and 53.1%, respectively (Supporting Information Fig. S4).

3.2. Antiviral assay

Next, the *in vitro* antiviral activities of schaftoside, vicenin-2, and licoisoflavanone against SARS-CoV-2 were measured in Vero E6 cells. The cells were inoculated with SARS-CoV-2 virus at a multiplicity of infection (MOI) of 0.01. At 24 h post-infection (dpi), viral RNA was extracted and determined by qRT-PCR. Schaftoside and licoisoflavanone showed remarkable antiviral
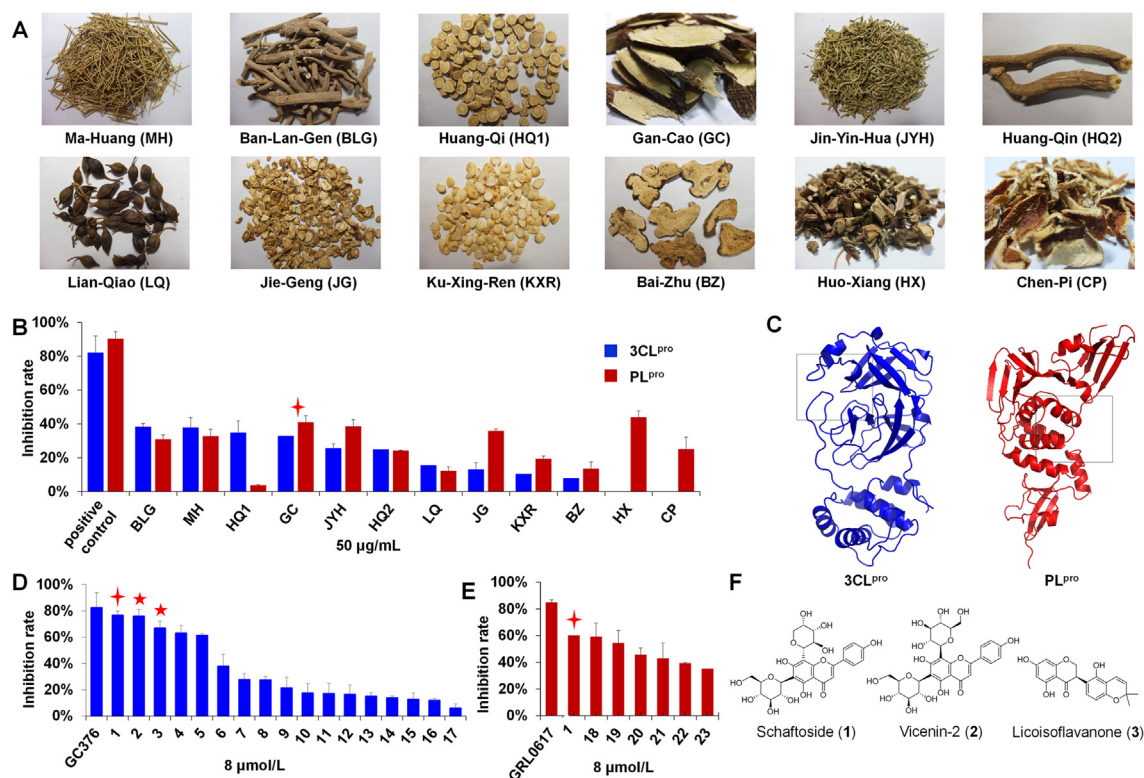

Figure 1 The inhibitory activities against severe acute respiratory syndrome coronavirus 2 (SARS-CoV-2) 3-chymotrypsin-like protease (3CL^{pro}) and papain-like protease (PL^{pro}) of traditional Chinese medicine herbs and compounds ($n = 3$). (A) Pictures of the 12 herbs. (B) The inhibitory activities against 3CL^{pro} and PL^{pro} of herbal extracts (50 μg/mL). (C) Active pockets of 3CL^{pro} and PL^{pro} for virtual screening. (D) The inhibitory activities against 3CL^{pro} of licorice compounds (8 μmol/L). (E) The inhibitory activities against PL^{pro} of licorice compounds (8 μmol/L). (F) Chemical structures of hit compounds **1–3**. For structures of the other compounds, see Supporting Information Fig. S3.
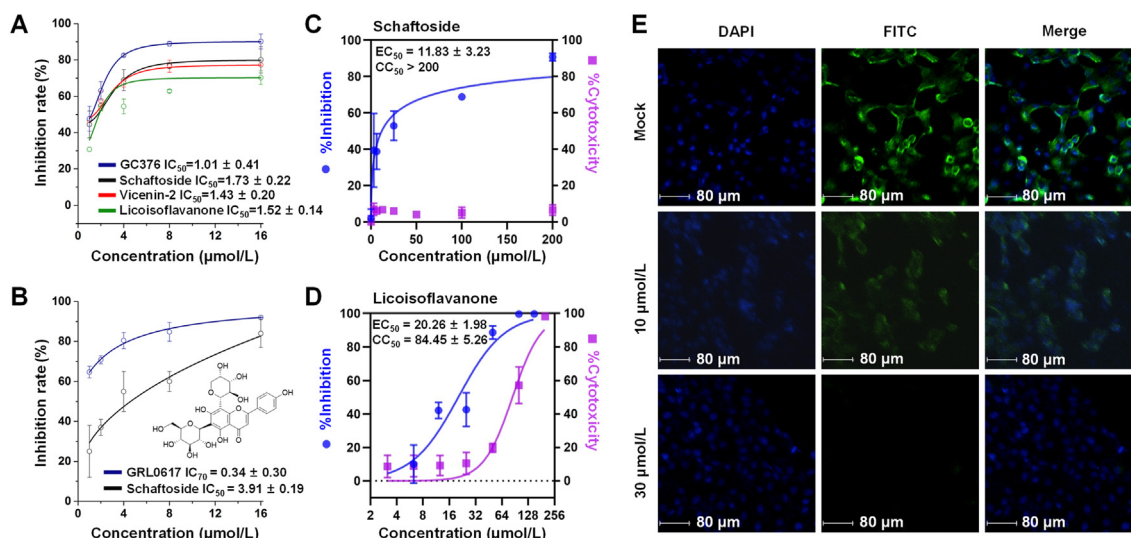
Figure 2 Inhibitory activity profiles of licorice compounds against SARS-CoV-2 3CL^{pro} and PL^{pro}, and antiviral activities of schaftoside against SARS-CoV-2 in Vero E6 cells. (A, B) Half maximal inhibitory concentrations (IC$_{50}$) against 3CL^{pro} and PL^{pro}. Data are shown as mean $\pm$ standard deviation, $n = 3$. GC376 and GRL0617 are the positive drugs for 3CL^{pro} and PL^{pro}, respectively. (C, D) Dose-dependent inhibition of schaftoside and licoisoflavanone against SARS-CoV-2 infection, $n = 3$. Cytotoxicities were determined by CCK-8 assay. Data are shown as mean $\pm$ standard deviation. (E) Immunofluorescence assay analysis of the inhibition of schaftoside against SARS-CoV-2 viral replication.

activities with EC$_{50}$ of 11.83 ± 3.23 and 20.26 ± 1.98 μmol/L, respectively (Fig. 2C and D). Vicenin-2 only showed weak activities, with an inhibition rate of around 40% at 30 μmol/L (Supporting Information Fig. S5). Given that licoisoflavanone showed obvious cytotoxicity with CC$_{50}$ of 84.45 μmol/L, schaftoside was considered as the most promising inhibitor among the 125 licorice compounds. An indirect immunofluorescence assay was conducted to verify the antiviral effects. As shown in Fig. 2E, schaftoside inhibited the replication of SARS-CoV-2 in a dose-dependent manner, when compared to the drug-free mock cells.

3.3. Binding mechanisms of schaftoside with 3CL^{pro} and PL^{pro}

To elucidate the binding mechanisms of schaftoside with 3CL^{pro} and PL^{pro}, we conducted SPR analysis. The results indicate that schaftoside binded to 3CL^{pro} and PL^{pro} with K_D values of 12.4 and 13.2 μmol/L, respectively (Supporting Information Fig. S6). Then, HDX-MS analysis was conducted to determine protein conformation changes due to interactions between 3CL^{pro} and schaftoside. After co-incubation with schaftoside, peptides 182−205, 35−57, 160−177, and 141−150 of 3CL^{pro} demonstrated 0.89, 0.54, 0.19 and 0.15 Da m/z loss, respectively (Fig. 3A). To further determine the specific binding sites (Fig. 3B), we solved the crystal structure of 3CL^{pro} (PDB ID: 7V7M, 2.08 Å) (Supporting Information Tables S6), and simulated the schaftoside/3CL^{pro} complex structure by molecular docking (Fig. 3C). The complex of schaftoside and the active sites (Fig. S2)[6] was then computed by the QM/MM method. The calculated interaction energy of schaftoside with SARS-CoV-2 3CL^{pro} residues was −32.6 kcal/mol (Fig. 3D). The strong binding may be due to the hydrogen bonding between 7-OH of schaftoside and the nitrogen atom of H41. The C8-arabinosyl moiety could interact with R188 through hydrogen bonding, and the C6-glucosyl moiety could bind to G143 and C145 through two hydrogen bonds. Moreover, 4′-OH of schaftoside could form a hydrogen bond with C=O of Q192.

To verify the above key amino acid residues, we conducted site-directed mutagenesis of SARS-CoV-2 3CL^{pro}. The Michaelis constants (K_m) of 3CL^{pro} mutants hydrolyzing the commercial substrate were measured (Supporting Information Fig. S7). For the H41A mutant, schaftoside showed an inhibition rate of 50.9%, which was remarkably lower than with the wild type (67.5%) (Fig. 3E). For the G143A and R188A mutants, the inhibition rates decreased substantially to 32% and 40.3%, respectively. These data were consistent with SPR measurements (Fig. S6). We further tested the inhibitory activities of schaftoside analogs GC1-GC4 (Supporting Information Fig. S8). When the 4′-OH group was absent, or only one C-glucosyl residue was substituted at the flavone aglycone, the inhibitory activities decreased to 15.2%− 46.1% (Fig. 3E). These results support our proposed mechanisms.

Likewise, HDX-MS analysis indicated the peptides 143−158 and 244−263 of PL^{pro} showed 0.15 and 0.26 Da m/z loss, respectively, upon the treatment of schaftoside (Fig. 3F and G). In molecular docking, A246 and E167 could interact with the C6-glucosyl moiety through hydrogen bonding, and K157 could bind to the C8-arabinosyl moiety through one hydrogen bond. In addition, 7-OH of schaftoside could form two hydrogen bonds with E167 and Y268 (Fig. 3H)[10]. These bindings were verified by QM/MM calculations (Supporting Information Fig. S9). The interaction energy of schaftoside with key residues K157, E167, A246 and Y268 was −22.5 kcal/mol (Fig. 3I).

Site-directed mutagenesis of SARS-CoV-2 PL^{pro} K157A, E167A and Y268A was conducted, and K_m and K_D values of PL^{pro} mutants were calculated (Fig. S6 and Supporting Information Fig. S10). Schaftoside could bind to all the three mutants, though around four times weaker with Y268A than with the wild type (Fig. S6). Consistently, schaftoside showed a low inhibitory activity against Y268A, with an inhibition rate of 33.7%. Meanwhile, the inhibitory activities of schaftoside with K157A and E167A decreased to 52.3% and 53.3%, respectively. These results indicate that Y268, K157 and E167 are critical residues for
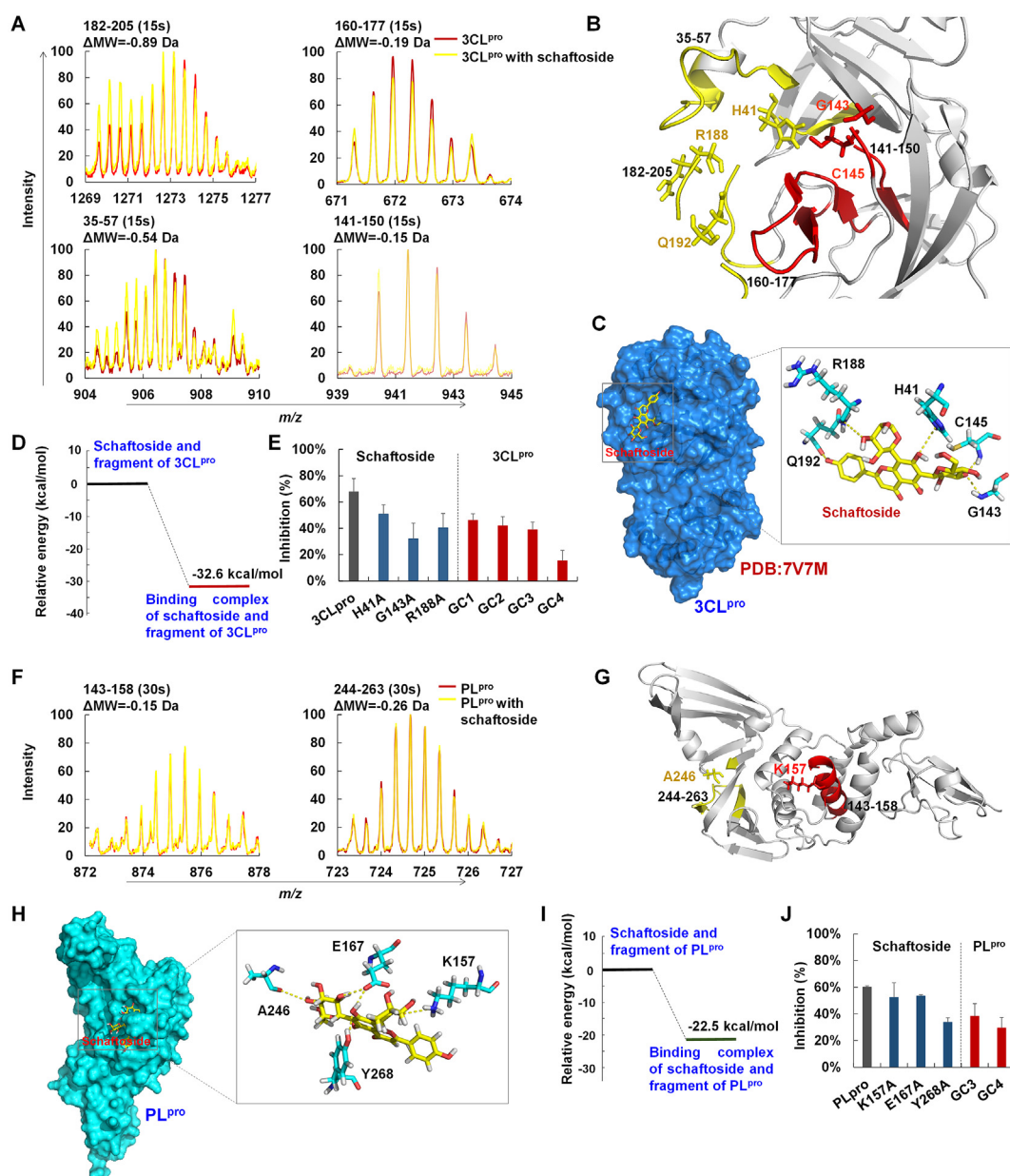
Figure 3 Binding mechanisms of schaftoside with 3CL^{pro} and PL^{pro}. (A) Mass spectra of peptides 182−205 and 35−57 (15 s) of 3CL^{pro} and 3CL^{pro} with schaftoside determined by hydrogen−deuterium exchange mass spectrometry (HDX-MS). (B) Location of peptides 35−57, 182−205, and 141−150 in 3CL^{pro}. (C) The crystal structure of 3CL^{pro} (PDB ID: 7V7M), and the binding mode of schaftoside with active residues of 3CL^{pro} by molecular docking. Hydrogen bonds (yellow dashes) are formed between schaftoside and residues H41, R188, Q192, G143 and C145 of 3CL^{pro}. (D) Relative energy of schaftoside with 3CL^{pro} computed by quantum mechanics/molecular mechanics (QM/MM). (E) Inhibitory activities of schaftoside (8 μmol/L) against SARS-CoV-2 3CL^{pro} and 3CL^{pro} mutants, and of flavonoid *C*-glycosides GC1, GC2, GC3 and GC4 (8 μmol/L) against SARS-CoV-2 3CL^{pro}. SARS-CoV-2 3CL^{pro} and 3CL^{pro} mutants were expressed and purified by our laboratory. (F) Mass spectra of peptides 143−158 and 244−263 (15 s) of PL^{pro} and PL^{pro} treated with schaftoside determined by HDX-MS. (G) Location of peptides 143−158 and 244−263 in PL^{pro}. (H) Binding mode of schaftoside with active residues of PL^{pro} by molecular docking. Hydrogen bonds (yellow dashes) are formed between schaftoside and residues K157, E167, A246 and Y268 of 3CL^{pro}. (I) Relative energy of schaftoside with PL^{pro} computed by QM/MM. (J) Inhibitory activities of schaftoside (8 μmol/L) against SARS-CoV-2 PL^{pro} and PL^{pro} mutants, and of flavonoid *C*-glycosides GC3 and GC4 (8 μmol/L) against SARS-CoV-2 PL^{pro}.

binding with schaftoside. For schaftoside analogs GC3 and GC4, where only one *C*-glucosyl residue is substituted at the flavone aglycone, the inhibitory activities against PL^{pro} decreased to 38.2% and 29.5%, respectively (Fig. 3J). The above data are consistent with our proposed mechanisms.

3.4. Proteomic variations of SARS-CoV-2-infected host cells treated with schaftoside

In order to understand the impact of schaftoside on the host cells, we conducted quantitative proteome analysis of the Vero E6 cells

treated with SARS-CoV-2 coupled with 30 μmol/L schaftoside for 24 h (Fig. 4A). A total of 842 up-regulated and 189 down-regulated proteins were identified (fold change > 1.3). Then we performed enrichment analyses of biological processes based on Gene Ontology (GO) annotations ($P < 0.05$), and 174 up-regulated and 40 down-regulated proteins were related to immune system process (Supporting Information Figs. S11 and S12)[32]. In functional enrichment analysis, schaftoside treatment led to regulations of immune response (neutrophil mediated immunity, 25 up-regulated proteins) and inflammation (leukocyte migration, 11 down-regulated proteins) (Fig. 4B and C)[33,34]. Moreover, 60 other regulated proteins were related with leukocyte

activation and T cell differentiation (Supporting information Table S7).

It has been reported that T cell responses are induced after SARS-CoV-2 infection[35,36]. Moreover, the spike protein carries immunodominant epitopes against which humoral B cell responses are generated upon natural infection[37]. In these immune processes, cytokine storm can be caused by the overproduction of early response proinflammatory cytokines[38,39]. Our ELISA results show the levels of cytokines IL-1, TNF-α, IL-6, IL-1β, IL-8, IL-7, IFN-β, and IFN-γ in the SARS-CoV-2 infected host cells decreased remarkably upon the treatment of schaftoside (Fig. 4D). These results indicate that schaftoside regulated immune response
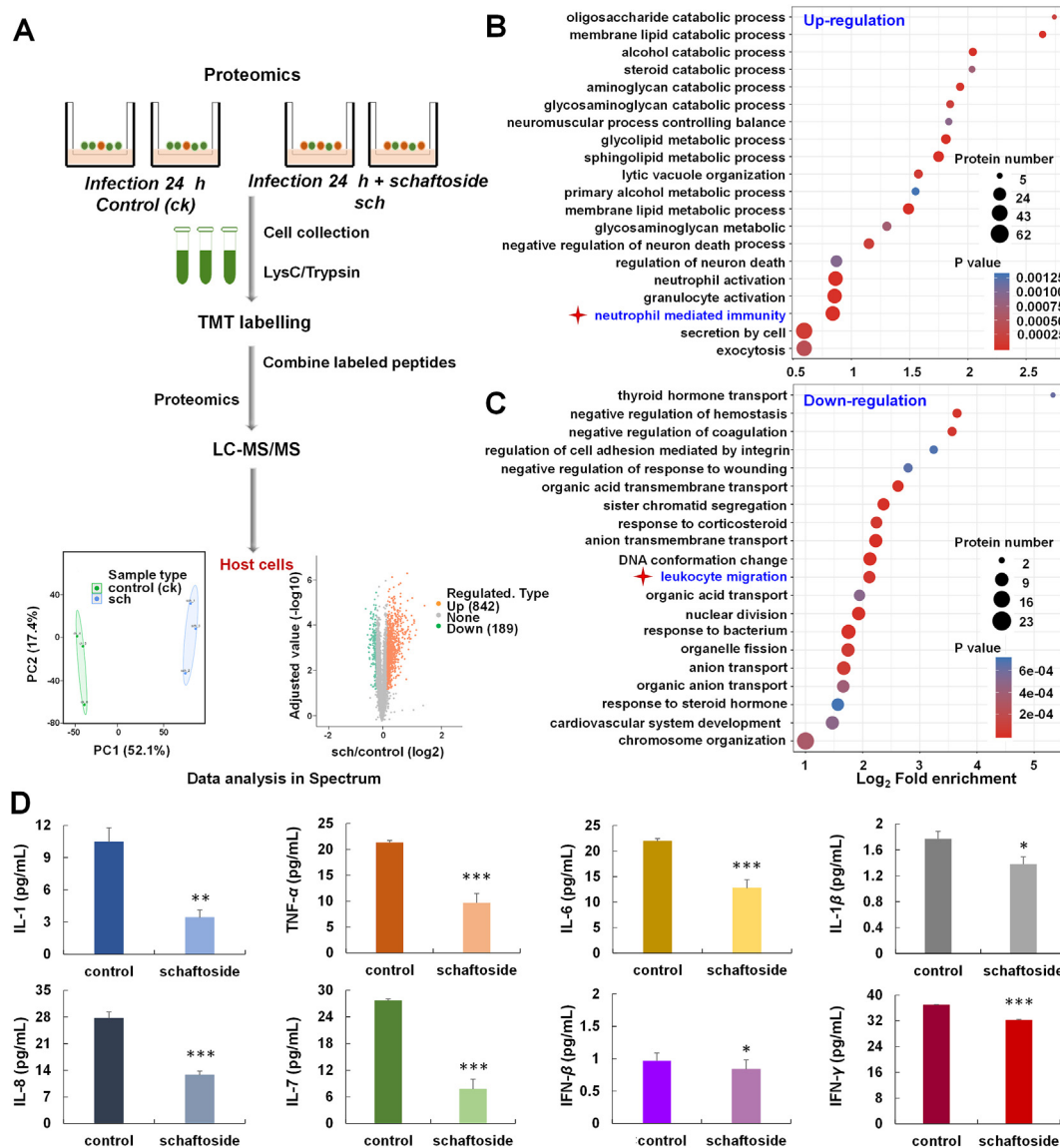

Figure 4 Proteomic profiling and cytokine levels of SARS-CoV-2 virus-infected Vero E6 cells upon schaftoside treatment. (A) Experimental scheme. Vero E6 cells were infected with SARS-CoV-2, or with schaftoside and SARS-CoV-2 for 24 h (MOI = 1), respectively. (B, C) The GO-based enrichment analysis of biologic processes that are differentially regulated by schaftoside (B, up-regulated; C, down-regulated). A two-tailed Fisher's exact test was employed to test the enrichment of the differentially expressed protein against all identified proteins ($P < 0.05$). (D) IL-1, TNF-α, IL-6, IL-1β, IL-8, IL-7, IFN-β and IFN-γ levels in Vero E6 cells measured by monkey ELISA kit. For the control group, Vero E6 cells were treated with SARS-CoV-2 for 24 h and were sonicated three times on ice using a high intensity ultrasonic processor (Scientz) in lysis buffer (8 mmol/L urea, 1% protease inhibitor cocktail). For the schaftoside group, Vero E6 cells were treated with schaftoside and SARS-CoV-2 for 24 h. *$P < 0.05$, **$P < 0.01$, ***$P < 0.001$ compared with the control group, $n = 3$.

and inflammation of the host cells. A proposed mechanism is shown in Supporting Information Fig. S13.

3.5. Anti-inflammatory activities of schaftoside in ALI mice model

To further evaluate the anti-inflammatory activities of schaftoside, an ALI mice model was established by intranasal (i.n.) administration of 2 mg/kg LPS (Fig. 5A)[40]. After 8 h LPS stimulation, histopathology of the lung tissue changed remarkably. The locally widened alveolar septum and perivascular areas were infiltrated by lymphocytes and neutrophils. Moreover, microvascular hyperpermeability could lead to alveolar wall thickening, alveolar space congestion, and alveolar edema (Fig. 5B and Supporting Information Fig. S14). These injuries were alleviated upon the treatment of schaftoside (10 and 20 mg/kg) (Fig. 5C). The levels of

proinflammatory cytokines TNF-α, IL-6, and IL-1β in mice blood samples decreased as well (Fig. 5D)[41], which were consistent with lung tissue IHC staining (Fig. 5E). These results confirm that schaftoside possessed remarkable anti-inflammatory activities, and could down-regulate inflammatory cytokines.

3.6. Druggability evaluation of schaftoside

The acute toxicity of schaftoside in mice was evaluated[42]. Male ICR mice (20 g) were treated with schaftoside (20, 40, and 300 mg/kg, i.g.) for 7 days, the mice weights remained at around 22 g without death (Supporting Information Fig. S15). No obvious histological changes were observed for the lung, heart, spleen, liver, and kidney tissues (Supporting Information Fig. S16). We also conducted a pharmacokinetic study of schaftoside in rats (i.p., 150 mg/kg). The maximum plasma concentration was
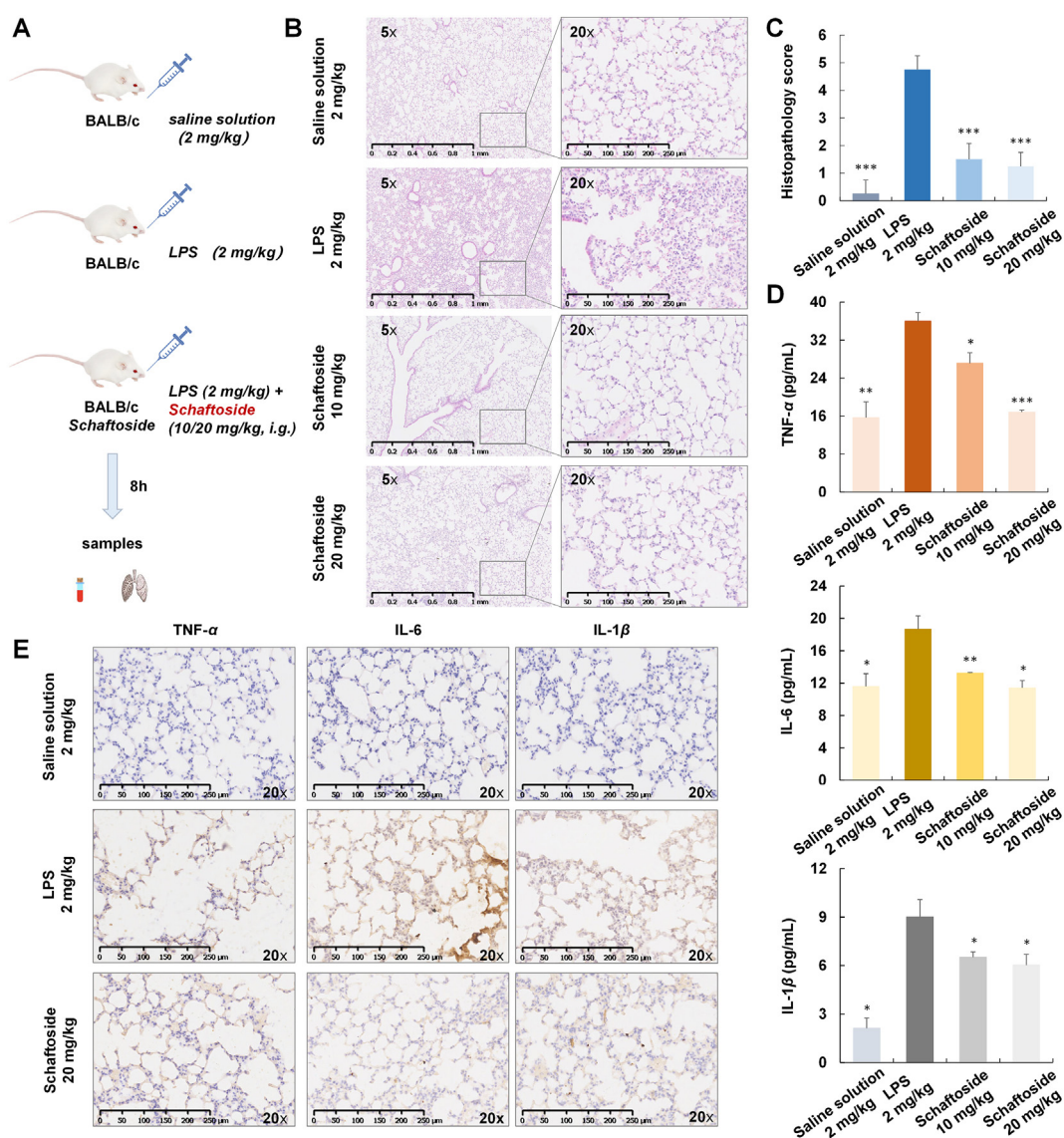

Figure 5 The anti-inflammatory activities of schaftoside on lipopolysaccharide (LPS)-induced acute lung injury (ALI) mice. (A) Experimental scheme[40]. (B) Effects of schaftoside (10 and 20 mg/kg, i.g.) on histological changes of the mice ($n = 4$). Representative images of mice lung tissue stained with HE after 8 h of LPS treatment. (C) Pathology evaluation for the therapeutic effect of schaftoside; $n = 4$ and ***$P < 0.001$[41]. (D) TNF-α, IL-6, and IL-1β levels of blood samples measured by mice ELISA kit. *$P < 0.05$, **$P < 0.01$, ***$P < 0.001$ compared with the control group, $n = 4$. (E) Immunohistochemistry of lung tissues of LPS-induced ALI mice for TNF-α, IL-6, and IL-1β analysis.

23.75 µmol/L, which was two-fold higher than the EC_{50} value (Supporting Information Fig. S17). The $t_{1/2}$ value of schaftoside was 7.5 h. The above results indicated that schaftoside showed little toxicity and good pharmacokinetic property.

4. Discussion

A number of small molecule inhibitors of SARS-CoV-2 virus $3CL^{pro}$ and PL^{pro} have been reported in the past two years. Most of these compounds were obtained by protein structure-based rational design and chemical synthesis. In this work, we focus on the discovery of natural products from Chinese herbal medicines that have been widely used in clinical practice for the treatment of COVID-19. By screening 12 popular herbal medicines and 125 compounds from licorice, we find that schaftoside is a potent $3CL^{pro}/PL^{pro}$ dual-target inhibitor, and could remarkably inhibit SARS-CoV-2 virus with EC_{50} of 11.83 ± 3.23 µmol/L. Molecular docking, HDX-MS analysis, and site-directed mutagenesis indicated the mechanisms may be related with non-covalent interactions. This mechanism is different from most previously reported $3CL^{pro}/PL^{pro}$ inhibitors, which could form covalent bonding with protein residues like cysteine. More importantly, we find that schaftoside not only inhibits the virus, but also regulates the immune response and inflammation of host cells infected with SARS-CoV-2, according to proteomics analysis and cytokine assay. The anti-inflammatory activity of schaftoside was further confirmed on an LPS-induced acute-lung injury mice model.

Schaftoside is a popular natural product (Supporting Information Figs. S18 and S19). It is present in at least 184 species of higher plants from 39 families, and the contents could be as high as 2.78%[43]. These plants include medicinal herbs like licorice and *Artemisia annua* L. (Qinghao), which are components of many traditional Chinese medicine formulas for the treatment of COVID-19. Recently, we have discovered key *C*-glycosyltransferases involved in the biosynthesis of schaftoside, and established efficient *in vitro* biosynthetic routes. Given its easy accessibility and good safety and pharmacokinetic property, schaftoside may be a promising drug candidate for the treatment of COVID-19.

5. Conclusions

Our previous study has found that glycyrrhetinic acid and licorice-saponin A3 from licorice could potently inhibit SARS-CoV-2 spike protein, with EC_{50} of 3.17 and 0.075 µmol/L against SARS-CoV-2 virus in Vero E6 cells[23], respectively. These compounds together with schaftoside are key effective components of licorice for the prevention and treatment of COVID-19. This work also demonstrates the multi-component, multi-target mode of action of herbal medicines.

Author contributions

Min Ye conceived this study. Yang Yi, Joachim Wlodarz and Szczepan Roszak conducted theoretical calculations. Yang Yi, Yi Kuang, Rong Yu and Yue Chai performed enzyme assay and pharmacokinetic (PK) studies. Heng Xue, Wei Hong, Junhua Li, Elishiba Muturi and Hongping Wei conducted antiviral and immunofluorescence assays. Meng Zhang, Yangoujie Bao and Yang Yi purified protein. Wen Ma conducted mass spectrometry analysis for PK experiments. Jing Wang completed SPR experiments. Xiaomeng Shi conducted hydrogen−deuterium exchange mass spectrometry analysis. Rong Yu and Yang Yi conducted anti-inflammation and toxicity tests in mice. Yang Yi and Wenzhe Li conducted immunohistochemistry analysis. Yang Yi, Xue Qiao, Hang Yang and Min Ye analyzed the data and wrote the manuscript.

Conflicts of interest

The authors declare no conflicts of interest.

Appendix A.   Supporting information

Supporting data to this article can be found online at https://doi.org/10.1016/j.apsb.2022.07.017.

References

1. Huang CL, Wang YM, Li XW, Ren LL, Zhao JP, Hu Y, et al. Clinical features of patients infected with 2019 novel coronavirus in Wuhan, China. *Lancet* 2020;**395**:497−506.
2. World Health Organization. *WHO coronavirus (COVID-19) dashboard*. World Health Organization; 2022-06-15. Available from: https://covid19.who.int.
3. Kimura I, Kosugi Y, Wu JQ, Yamasoba D, Butlertanaka EP, Tanaka YL, et al. SARS-CoV-2 lambda variant exhibits higher infectivity and immune resistance. *BioRxiv* 2021. Available from: https://doi.org/10.1101/2021.07.28.454085.
4. Su HX, Yao S, Zhao WF, Zhang YM, Liu J, Shao Q, et al. Identification of pyrogallol as a warhead in design of covalent inhibitors for the SARS-CoV-2 3CL protease. *Nat Commun* 2021;**12**:3623.
5. Ramajayam R, Tan KP, Liang PH. Recent development of 3C and 3CL protease inhibitors for anti-coronavirus and anti-picornavirus drug discovery. *Biochem Soc Trans* 2011;**39**:1371−5.
6. Dai WH, Zhang B, Jiang XM, Su HX, Jian Li, Zhao Y, et al. Structure-based design of antiviral drug candidates targeting the SARS-CoV-2 main protease. *Science* 2020;**368**:1331−5.
7. Fu LF, Ye F, Feng Y, Yu F, Wang QS, Wu Y, et al. Both boceprevir and GC376 efficaciously inhibit SARS-CoV-2 by targeting its main protease. *Nat Commun* 2020;**11**:4417.
8. Qiao JX, Li YS, Zeng R, Liu FL, Luo RH, Huang C, et al. SARS-CoV-2 M^{pro} inhibitors with antiviral activity in a transgenic mouse model. *Science* 2021;**371**:1374−8.
9. Owen DR, Allerton CMN, Anderson AS, Aschenbrenner L, Avery M, Berritt S, et al. An oral SARS-CoV M^{pro} inhibitor clinical candidate for the treatment of COVID-19. *Science* 2021;**24**:1586−93.
10. Fu ZY, Huang B, Tang JL, Liu SY, Liu M, Ye YX, et al. The complex structure of GRL0617 and SARS-CoV-2 PL^{pro} reveals a hot spot for antiviral drug discovery. *Nat Commun* 2021;**12**:488.

11. Gao XP, Qin B, Chen P, Zhu KX, Hou PJ, Wojdyla JA, et al. Crystal structure of SARS-CoV-2 papain-like protease. *Acta Pharm Sin B* 2021;**11**:237−45.

12. Osipiuk J, Azizi SA, Dvorkin S, Endres M, Jedrzejczak R, Jones KA. Structure of papain-like protease from SARS-CoV-2 and its complexes with non-covalent inhibitors. *Nat Commun* 2021;**12**:743.

13. Medicines and Healthcare products Regulatory Agency. *First oral antiviral for COVID-19, Lagevrio (molnupiravir), approved by MHRA*. GOV.UK; 2021-11-04. Available from: https://www.gov.uk/government/news/first-oral-antiviral-for-covid-19-lagevrio-molnupiravir-approved-by-mhra.

14. Pfizer. *Pfizer receives U.S. FDA emergency use authorization for novel COVID-19 oral antiviral treatment*. Pfizer; 2021-12-22. Available from: https://www.pfizer.com/news/press-release/press-release-detail/pfizer-receives-us-fda-emergency-use-authorization-novel.

15. Merck. *Merck and ridgeback's molnupiravir, an oral COVID-19 antiviral medicine, receives first authorization in the world*. MERCK; 2021-11-04. Available from: https://www.merck.com/news/merck-and-ridgebacks-molnupiravir-an-oral-covid-19-antiviral-medicine-receives-first-authorization-in-the-world.

16. Pfizer. *Pfizer to provide U.S. government with 10 million treatment courses of investigational oral antiviral candidate to help combat COVID-19*. worldpharmanews; 2021-11-18. Available from: https://www.worldpharmanews.com/pfizer/5863-pfizer-to-provide-u-s-government-with-10-million-treatment-courses-of-investigational-oral-antiviral-candidate-to-help-combat-covid-19.

17. Hu K, Guan WJ, Bi Y, Zhang W, Li LJ, Zhang BL, et al. Efficacy and safety of Lianhuaqingwen capsules, a repurposed Chinese herb, in patients with coronavirus disease 2019: a multicenter, prospective, randomized controlled trial. *Phytomedicine* 2021;**85**:153242.

18. Zhang LH, Zheng X, Bai XK, Wang Q, Chen BW, Qang HB, et al. Association between use of Qingfei Paidu Tang and mortality in hospitalized patients with COVID-19: a national retrospective registry study. *Phytomedicine* 2021;**85**:153531.

19. Chen XF, Wu YL, Chen C, Gu YQ, Zhu CY, Wang SP, et al. Identifying potential anti-COVID-19 pharmacological components of traditional Chinese medicine Lianhuaqingwen Capsule based on human exposure and ACE2 biochromatography screening. *Acta Pharm Sin B* 2021;**11**:222−36.

20. Yang C, Pan XY, Xu XF, Cheng C, Huang Y, Li L, et al. Salvianolic acid C potently inhibits SARS-CoV-2 infection by blocking the formation of six-helix bundle core of spike protein. *Signal Transduct Target Ther* 2020;**5**:220.

21. Suresh G, Badavath VN, Thakur A, Yin N, De Jonghe S, Acevedo O, et al. Kobophenol A inhibits binding of host ACE2 receptor with spike RBD domain of SARS-CoV-2, a lead compound for blocking COVID-19. *J Phys Chem Lett* 2021;**12**:1793−802.

22. Ji S, Li ZW, Song W, Wang YR, Liang WF, Li K, et al. Bioactive constituents of *Glycyrrhiza uralensis* (licorice): discovery of the effective components of a traditional herbal medicine. *J Nat Prod* 2016;**79**:281−92.

23. Yi Y, Li JH, Lai XY, Zhang M, Kuang Y, Bao YOJ, et al. Natural triterpenoids from licorice potently inhibit SARS-CoV-2 infection. *J Adv Res* 2022;**36**:201−10.

24. Wang LL, Chen K, Wang ZL, Yi Y, Zhang M, Hasan A, et al. AmAT19, an acetyltransferase from *Astragalus membranaceus*, catalyses specific 6α-OH acetylation for tetracyclic triterpenes and steroids. *Org Biomol Chem* 2021;**19**:7186−9.

25. McLean AD, Chandler GS. Contracted Gaussian-basis sets for molecular calculations. *J Chem Phys* 1980;**72**:5639−48.

26. Lee C, Yang W, Parr RG. Development of the Colle-Salvetti correlation-energy formula into a functional of the electron density. *Phys Rev B* 1988;**37**:785−9.

27. Becke AD. Density-functional thermochemistry. III. The role of exact exchange. *J Chem Phys* 1993;**98**:5648−52.

28. Morris GM, Huey R, Lindstrom W, Sanner MF, Belew RK, Goodsell DS, et al. AutoDock4 and AutoDockTools4: automated docking with selective receptor flexibility. *J Comput Chem* 2009;**30**:2785−91.

29. Rappe AK, Casewit CJ, Colwell KS, III Goddard WA, Skiff WMJ. UFF. A full periodic table force field for molecular mechanics and molecular dynamics simulations. *J Am Chem Soc* 1992;**114**:10024−35.

30. Frisch M.J., Trucks G.W., Schlegel H.B., Scuseria G.E., Robb M.A., Cheeseman J.R., et al. Gaussian 09, revision E.01, Inc., Wallingford. 2013. Available from: https://gaussian.com.

31. Luo L, Jiang JW, Wang C, Fitzgerald M, Hu WF, Zhou YM, et al. Analysis on herbal medicines utilized for treatment of COVID-19. *Acta Pharm Sin B* 2020;**10**:1192−204.

32. Subramanian A, Tamayo P, Mootha VK, Mukherjee S, Ebert BL, Gillette MA, et al. Geneset enrichment analysis: a knowledge-based approach for interpreting genome-wide expression profiles. *Proc Natl Acad Sci U S A* 2005;**102**:15545−50.

33. Nomani M, Varahram M, Tabarsi P, Hashemian SM, Jamaati H, Malekmohammad M, et al. Decreased neutrophil-mediated bacterial killing in COVID-19 patients. *Scand J Immunol* 2021;**94**:e13083.

34. Xu G, Qi FR, Li HJ, Yang QT, Wang HY, Wang X, et al. The differential immune responses to COVID-19 in peripheral and lung revealed by single-cell RNA sequencing. *Cell Disc* 2020;**6**:73.

35. Breton G, Mendoza P, Hagglof T, Oliveira TY, Schaefer-Babajew D, Gaebler C, et al. Persistent cellular immunity to SARS-CoV-2 infection. *bioRxiv* 2021. Available from: https://doi.org/10.1101/2020.12.08.416636.

36. Sette A, Crotty S. Adaptive immunity to SARS-CoV-2 and COVID-19. *Cell* 2021;**184**:861−80.

37. Ni L, Ye F, Cheng M, Feng Y, Deng YQ, Zhao H, et al. Detection of SARS-CoV-2-specific humoral and cellular immunity in COVID-19 convalescent individuals. *Immunity* 2020;**52**:971−7.

38. Zhou F, Yu T, Du RH, Fan GH, Liu Y, Liu ZB, et al. COVID-19 cytokine storm: the interplay between inflammation and coagulation. *Lancet* 2020;**395**:1054−62.

39. van de Veerdonk FL, Giamarellos-Bourboulis E, Pickkers P, Derde L, Leavis H, van Crevel R, et al. A guide to immunotherapy for COVID-19. *Nat Med* 2022;**28**:39−50.

40. Bai ZF, Li PY, Wen JC, Han YZ, Cui YY, Zhou YF, et al. Inhibitory effects and mechanisms of the anti-COVID-19 traditional Chinese prescription, Keguan-1, on acute lung injury. *J Ethnopharmcol* 2022;**285**:114838.

41. Szarka RJ, Wang ND, Gordon L, Nation PN, Smith RH. A murine model of pulmonary damage induced by lipopolysaccharide *via* intranasal instillation. *J Immunol Methods* 1997;**202**:49−57.

42. Chang X, Dong M, Mi X, Hu M, Lu J, Chen X. The protective effect of *Trichilia catigua* A. Juss. on DEHP-induced reproductive system damage in male mice. *Front Pharmacol* 2022;**13**:832789.

43. Wang ZL, Gao HM, Wang S, Zhang M, Chen K, Zhang YQ, et al. Dissection of the general two-step di-*C*-glycosylation pathway for the biosynthesis of (iso)schaftosides in higher plants. *Proc Natl Acad Sci U S A* 2020;**117**:30816−23.